nature communications

Article

https://doi.org/10.1038/s41467-026-69307-1

Dual spillover of carbon monoxide and hydrogen initiates tandem urea electrosynthesis

Received: 29 June 2025

Accepted: 20 January 2026

Published online: 07 February 2026

Check for updates

Yuefei Li[1,6], Bingying Han[2,6], Yurong Liu[2,6], Ye Liu[2], Riguang Zhang[2], Baojun Wang[2], Yu Chen[3] ✉, Bao Yu Xia[4,5] ✉ & Jiayuan Li[1] ✉

Electrochemical urea synthesis from CO_2 and NO_3^- provides a sustainable alternative to industrial processes, yet remains challenged by inefficient C-N coupling and protonation. Here, we present a tandem urea electrosynthesis pathway over copper-supported palladium hydride (PdH_x/Cu) through a dual spillover of CO* and H*. This pathway undergoes efficient CO_2-to-CO* conversion on PdH_x and facile NO_3^--to-NO* conversion on Cu. Crucially, rapid spillover of CO* (from PdHx surface) and H* (from PdH_x lattice) to Cu facilitates key C-N intermediate (OCNO*) formation and protonation, respectively. Our catalysts demonstrated high performance, achieving a urea production rate of 236.5 ± 8.9 mmol g_{cat}^{-1} h^{-1} with a Faradaic efficiency for urea of $62.6 \pm 1.8\%$. With these catalysts, our scaled-up flow cell enabled continuous co-production of urea and formate with consistent profitability and much lower CO_2 emissions compared to these for the present-day urea production route. This achievement represents a significant step for sustainable urea production.

Urea, a critical nitrogen fertilizer that supports ~40% of global agricultural productivity, is recognized as one of the most essential chemicals[1,2]. In industry, urea production relies heavily on upstream ammonia synthesis via the Haber-Bosch process and hydrogen generation through steam methane reforming—both of which are associated with high energy consumption and considerable CO_2 emissions[3,4]. Electrocatalytic urea synthesis utilizing nitrate (NO_3^-) pollutants—or NO_3^- obtained via sustainable plasma activation of N_2—along with CO_2 from anthropogenic activities, simultaneously mitigates environmental pollution and enables sustainable chemical production, offering a promising alternative strategy[5–11]. However, the intricate multistep reaction mechanism of urea electrosynthesis that involves a 16-electron transfer presents significant limitations in urea production and induces severe side reactions[12–14]. Consequently, the rational design and development of electrocatalysts with high performance is urgently required.

The C-N intermediate formation (e.g., OCNO*) and protonation are the key elementary steps in urea electrosynthesis[7,15–19]. Despite extensive efforts, simultaneously optimizing these substeps on a single catalyst remains highly challenging due to scaling relations that correlate the adsorption free energies of relevant C-N intermediates and their protonated species[7,15–19]. This correlation often leads to suboptimal urea production efficiency. Tandem catalysts, which spatially separate the C-N coupling and protonation steps onto distinct components and facilitate the transport of intermediates between them, offer a promising strategy to independently tailor the adsorption

[1]Key Laboratory of Special Functional and Smart Polymer Materials of Ministry of Industry and Information Technology, School of Chemistry and Chemical Engineering, Northwestern Polytechnical University, Xi'an, China. [2]State Key Laboratory of Clean and Efficient Coal Utilization, Taiyuan University of Technology, Taiyuan, China. [3]Key Laboratory of Applied Surface and Colloid Chemistry (Ministry of Education), School of Materials Science and Engineering, Shaanxi Normal University, Xi'an, China. [4]State Key Laboratory of New Textile Materials and Advanced Processing, Key Laboratory of Material Chemistry for Energy Conversion and Storage (Ministry of Education), Hubei Key Laboratory of Material Chemistry and Service Failure, School of Chemistry and Chemical Engineering, Huazhong University of Science and Technology (HUST), Wuhan, P. R. China. [5]Center for Next-Generation Energy Materials, School of Chemical Engineering, Sungkyunkwan University (SKKU), Suwon, Gyeonggi-do, Republic of Korea. [6]These authors contributed equally: Yuefei Li, Bingying Han, Yurong Liu. ✉e-mail: ndchenyu@gmail.com; byxia@hust.edu.cn; Jiayuanli@nwpu.edu.cn

behavior of key species[12,18]. However, the remote distance between C-N coupling sites and protonation sites, combined with the significant steric hindrance of C-N intermediates, hinders efficient C-N intermediate transfer and subsequent protonation. As a result, the overall urea production efficiency often falls short of expectations. Therefore, the design of tandem urea electrosynthesis catalysts with a better reaction path to overcome the above challenges is highly desirable.

In this work, we propose an optimized tandem urea electrosynthesis pathway, leveraging dual spillover of the sterically unhindered CO* and H* intermediates. Palladium hydrides (PdH_x) are paired with copper (Cu) to separate efficient CO_2-to-CO* and NO_3^--to-NO* conversions on PdH_x and Cu, respectively. CO* spillover from PdH_x surface to Cu facilitates the first C-N coupling (intermediate OCNO*), while H* spillover from PdH_x lattice to Cu promotes the protonation of the resulting C-N intermediates. Our catalyst system achieved a high urea production rate (r_{urea}) of 236.5 ± 8.9 mmol g_{cat}^{-1} h^{-1} with a Faradaic efficiency (FE_{urea}) of 62.6 ± 1.8% at − 0.7 V vs. RHE. To demonstrate practical applicability, we designed an enlarged two-electrode flow cell using PdH_x/Cu catalysts as both the cathode and anode. This system enabled continuous urea electrosynthesis at the cathode and methanol-to-formate conversion at the anode, operating stably over 200 h with high efficiency (470.5 ± 30.1 mmol g_{cat}^{-1} h^{-1} for urea and 2850.1 ± 51.1 mmol g_{cat}^{-1} h^{-1} for formic acid). A techno-economic analysis and life cycle assessment for this route indicated consistent profitability and significantly reduced CO_2 emissions, compared with these for the conventional route.

Results

Catalyst design

Current tandem catalysts for urea electrosynthesis typically consist of component (i) for efficient C-N coupling and component (ii) for facile C-N intermediate protonation (Fig. 1a). However, due to the restricted diffusion of these sterically hindered C-N intermediates (e.g., barrier: ~ 0.83 − 3.61 eV)[20,21], the successful transfer of C-N intermediates from component (i) to component (ii) is infrequent, severely limiting subsequent C-N protonation and thus urea electrosynthesis[12].

To address this limitation, we propose a tandem electrosynthesis pathway that leverages the efficient dual spillover of CO* and H* intermediates, which exhibit significantly reduced steric hindrance (Fig. 1b). In our design, metallic Cu with exposed (111) crystal planes is selected as component (ii) owing to its well-established selectivity in converting NO_3^- to NO* intermediates, along with its ability to accumulate NO* due to the high energy barrier associated with the NO* → N* step[22]. Subsequently, PdH_x is identified as the optimal choice for component (i) based on its dual functionality in enabling two efficient and non-interfering spillover processes: (i) surface-mediated CO* migration (e.g., barrier: ~ 0.16 eV)[23] and (ii) lattice-incorporated H* (de) intercalation (e.g., barrier: ~ 0.06 eV)[24]. In the resulting PdH_x/Cu hybrid system, CO* species generated on Pd surfaces undergo rapid migration to adjacent Cu surfaces through a well-documented spillover mechanism[25,26]. Concurrently, PdH_x phases serve as dynamic H* reservoirs, facilitating reversible (de)intercalation and subsequent H* spillover to neighboring Cu surfaces[27]. This design creates spatial proximity between spillover-derived CO* (CO_{Sp}*) and NO* species, thereby significantly enhancing their collision probability and accelerating C-N coupling. Furthermore, the close proximity of spillover-derived H* (H_{Sp}*) to the resulting C-N intermediates (e.g., OCNO*) ensures high collision probability, enabling efficient protonation of C-N intermediates. By simultaneously optimizing both C-N coupling and protonation processes through this dual spillover-driven tandem pathway, we anticipate that PdH_x/Cu hybrid catalysts exhibit high capability for significantly improving urea electrosynthesis performance.

Catalyst synthesis and characterization

Considering that Cu nanosheets offer a large surface area with exposed (111) crystal planes and that decorating them with PdH_x nanoparticles can generate abundant PdH_x–Cu heterogeneous interfaces[28,29], we synthesized PdH_x/Cu catalysts via a two-step wet-chemical method: (i) preparation of PdH_x nanoparticles, and (ii) synthesis of Cu nanosheets with simultaneous in situ loading of PdH_x. Through the inductively coupled plasma-mass spectrometry (ICP-MS), the weight loading of PdH_x in PdH_x/Cu catalysts was determined to be ~ 7.0 wt.% (Supplementary Table 1). The transmission electron microscopy (TEM) image revealed the uniform distribution of small nanoparticles (~ 3.81 nm) on the nanosheets (Fig. 2a). High-resolution TEM analysis revealed lattice

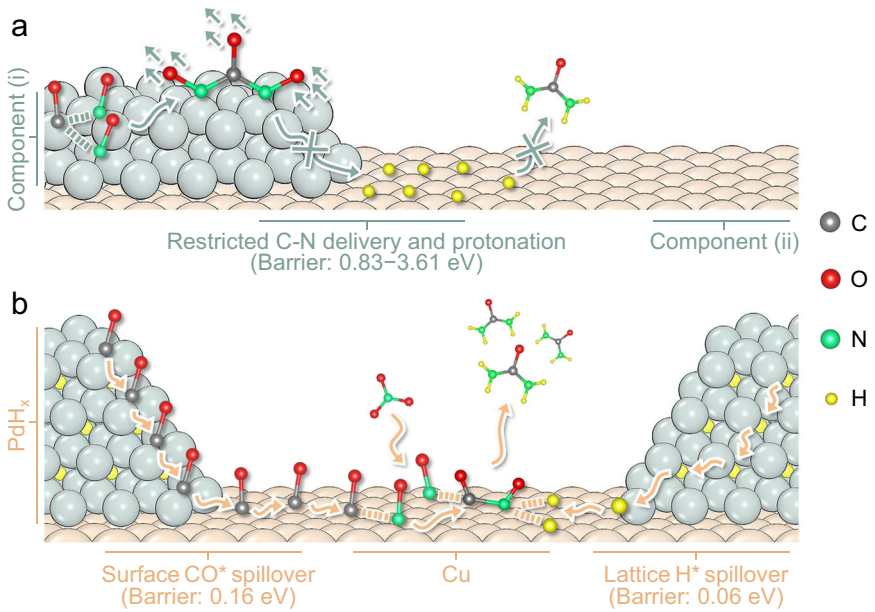

Fig. 1 | Design conception. a Schematic diagram of the conventional design conception for tandem urea electrosynthesis[12,18]. **b** Schematic diagram of our design conception for tandem urea electrosynthesis through dual CO* and H* spillover over the PdH_x/Cu catalysts. The energy barrier values are based on the previous results[20,21,23,24].

https://doi.org/10.1038/s41467-026-69307-1

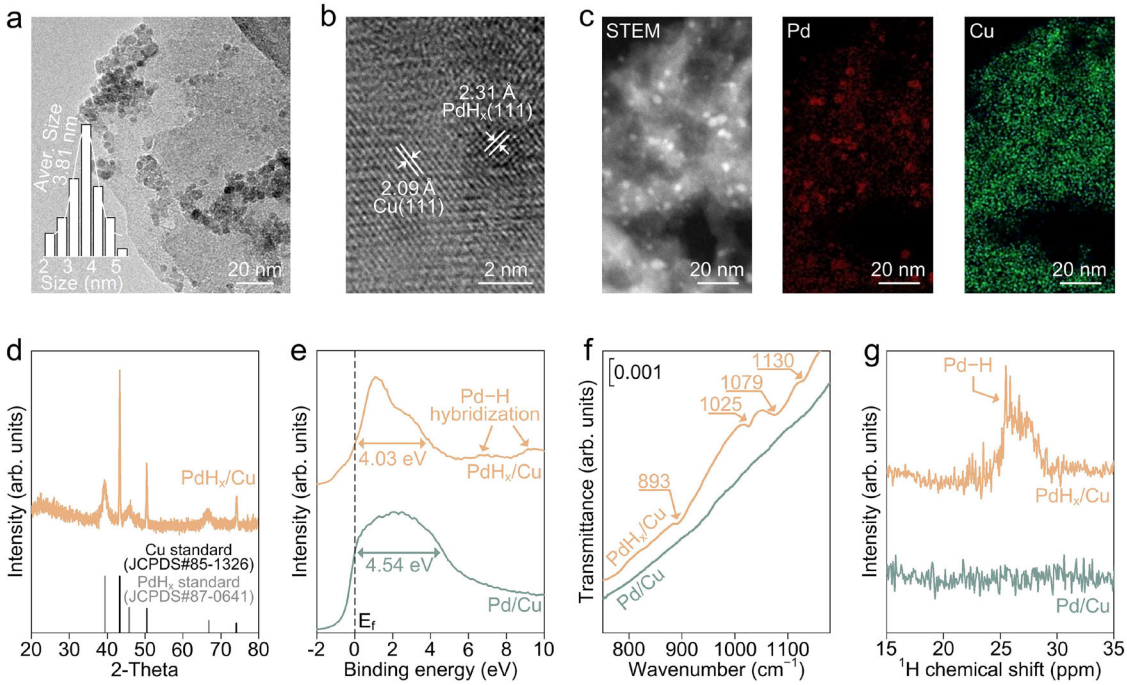

Fig. 2 | Characterizations of model catalysts. a TEM image of the PdH_x/Cu catalysts. **b** High-resolution TEM image of the PdH_x/Cu catalysts. **c** Elemental X-ray mapping of the PdH_x/Cu catalysts. **d** XRD pattern of the PdH_x/Cu catalysts. **e** XPS valence band of PdH_x/Cu and Pd/Cu. **f** FT-IR spectra of PdH_x/Cu and Pd/Cu. **g** ^{1}H ssNMR spectra of PdH_x/Cu and Pd/Cu.

spacings of 2.09 Å and 2.31 Å for the nanosheets and nanoparticles, respectively. The former corresponds to the (111) plane of bulk Cu[28], while the latter was consistent with the (111) spacing of the reported PdH_x (Fig. 2b)[30,31]. TEM elemental X-ray mapping revealed a concentrated distribution of Pd in the nanoparticles and a uniform distribution of Cu in the nanosheets (Fig. 2c). These results indicate the formation of PdH_x/Cu hybrids.

To get more evidences, multiple spectroscopic analyses were carried out and similar catalysts with Pd nanoparticles loaded on Cu nanosheets (Pd/Cu, Supplementary Fig. 1) were also prepared for comparison. The powder X-ray diffraction (XRD) pattern of PdH_x/Cu was indexed to standard PdH_x (JCPDS #87-0641) and Cu (JCPDS #85-1326) phases (Fig. 2d). The observed diffraction peak downshift of PdH_x/Cu relative to that of Pd/Cu is due to lattice expansion resulting from H intercalation in PdH_x[31]. The X-ray photoelectron spectroscopy (XPS) results indicated that Pd and Cu in both PdH_x/Cu and Pd/Cu are mainly in the metallic state (Supplementary Fig. 2). The Pd 3*d* peak of the PdH_x/Cu shift to higher binding energies by 0.3 eV compared with that of the Pd/Cu, demonstrating the electronic Pd−H interaction in PdH_x/Cu[32]. XPS valence-band spectra (Fig. 2e) revealed a narrower bandwidth for PdH_x/Cu compared to Pd/Cu, consistent with characteristic features of Pd hydride systems[31]. The appearance of ~ 6 and ~ 9 eV shake-up satellites in PdH_x/Cu indicates strong hybridization between Pd 4*d* and H 1*s* orbitals[33]. These results support the formation of PdH_x/Cu hybrids. The Fourier transform-infrared (FT-IR) transmission spectra were performed to examine the vibration of Pd−H in PdH_x lattice (Fig. 2f). Four new characteristic peaks located at 893, 1025, 1079, and 1130 cm^{-1} were observed for PdH_x/Cu compared with that for Pd/Cu. These peaks match well with those of the previously reported ones for Pd hydrides[32], confirming the successful formation of PdH_x in PdH_x/Cu. The ^{1}H solid-state nuclear magnetic resonance (ssNMR) analysis revealed the appearance of a new peak at ~ 26 ppm for PdH_x/Cu (Fig. 2g), which was absent for Pd/Cu. This again confirms the existence of a Pd−H bond in PdH_x[34]. CO stripping voltammetry further excluded the formation of Pd-Cu alloys on PdH_x/Cu surface, as reflected by the presence of two typical CO stripping peaks at ~ 0.52 and ~ 0.76 V vs. RHE, consistent with those of PdH_x and Cu benchmarks (Supplementary Fig. 3)[28,35]. All the above results confirm the successful synthesis of the PdH_x/Cu catalysts.

Catalytic evaluation

The catalytic performance for urea electrosynthesis from CO_2 and NO_3^- was investigated using a three-electrode flow cell (Supplementary Fig. 4). To better evaluate the performance of PdH_x/Cu, we then synthesized the Cu catalysts through similar synthetic strategy without addition of PdH_x (Supplementary Fig. 5). Linear sweep voltammetry (LSV) revealed that the PdH_x/Cu catalysts exhibited high urea electrosynthesis activity, as evidenced by the significantly higher current densities in the presence of both CO_2 and NO_3^- compared to environments missing either or both of these reactants (Supplementary Fig. 6). The urea production yield was driven by chronoamperometric conditions (applied potential range: − 0.4 to − 0.8 V vs. RHE) and the catalytic current density was extracted from the chronoamperometry profiles (Supplementary Fig. 7). A 95% on-the-fly iR compensation method was applied during these measurements[36], and neither the uncompensated nor the compensated chronoamperometry profiles exhibited potentiostat oscillations (Supplementary Fig. 8), confirming the appropriateness of the compensation protocol. The liquid and gas products were quantified using ^{1}H NMR spectroscopy and gas chromatography (GC). The PdH_x/Cu catalyst exhibited optimal urea electrosynthesis performance at − 0.7 V vs. RHE, achieving a Faradaic efficiency (FE_{urea}) of 62.6 ± 1.8% and a mass-normalized urea production rate (r_{urea}) of 236.5 ± 8.9 mmol g_{cat}^{-1} h^{-1} (Fig. 3a and see ^{1}H-NMR quantification details in Supplementary Fig. 9). These urea product quantification was further examined via spectrophotometric methods (see details in Methods section)[4,12], which was consistent with the results obtained from ^{1}H-NMR (Supplementary Fig. 10). Under identical conditions, the individual Cu showed significantly lower performance, with an r_{urea} of 19.8 ± 1.5 mmol g_{cat}^{-1} h^{-1} and FE_{urea} of 17.3 ± 0.8% (Fig. 3b and Supplementary Fig. 11). For both catalysts, no NO_2^-,

https://doi.org/10.1038/s41467-026-69307-1

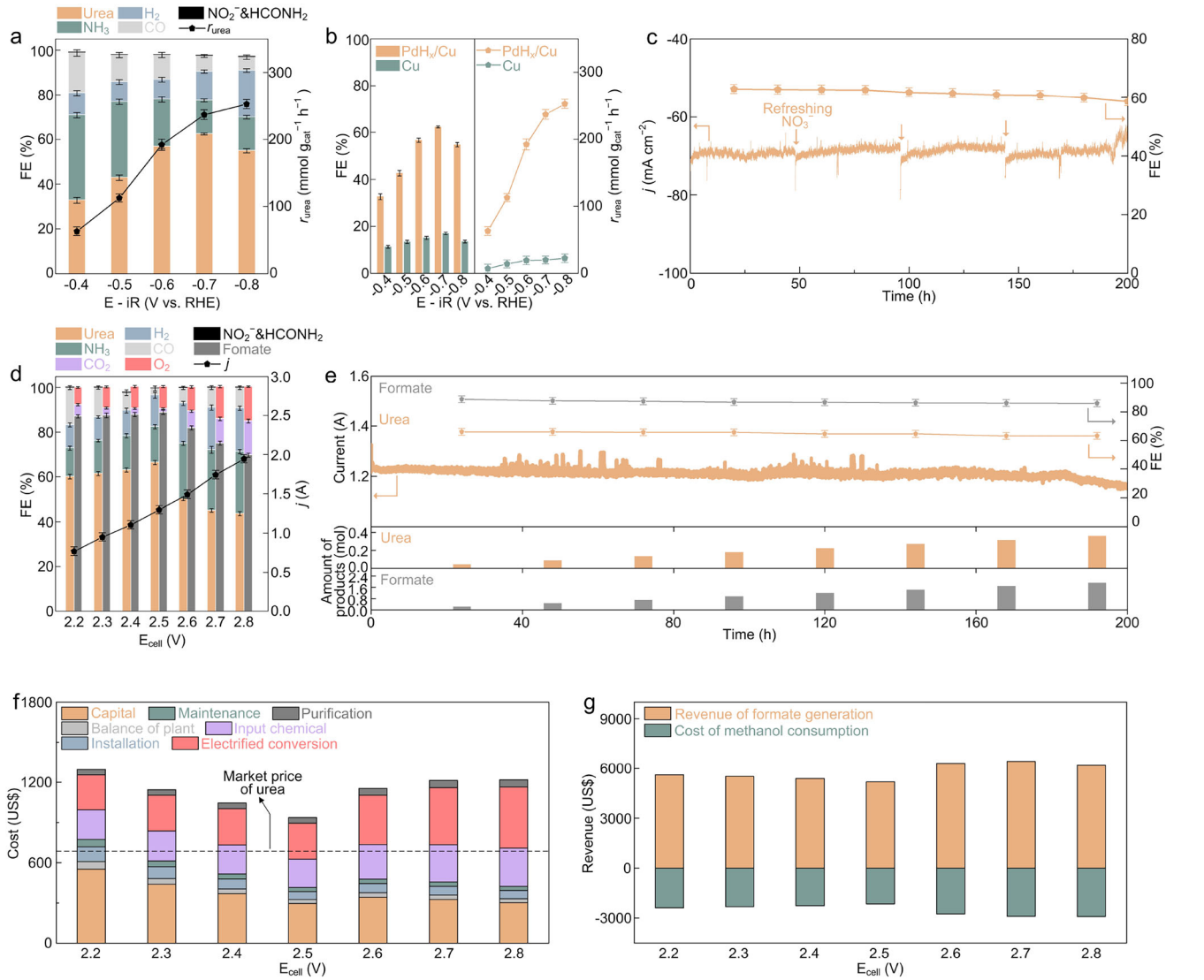

Fig. 3 | Catalytic evaluation. a FE distributions of the products and corresponding r_{urea} for PdH_x/Cu at different potentials. **b** Comparisons of urea electrosynthesis performance of PdH_x/Cu and Cu. **c** Durability and FE_{urea} of PdH_x/Cu through chronopotentiometry at − 0.7 V vs. RHE. **d** FE distributions of the products and corresponding *j* for PdH_x/Cu(+)||PdH_x/Cu(−) configuration at different E_{cell} values. **e** Continuous urea production at the cathode and formic acid production at the anode for 200 h. Every day, an appropriate amount of NO_3^- was added to the electrolyte. **f** Calculated cost for urea electrosynthesis in cthe athode over the flow cell with PdH_x/Cu(+)||PdH_x/Cu(−) electrode configuration at different E_{cell}. **g** Calculated revenue and cost for formate generation and methanol consumption in anode over the flow cell with PdH_x/Cu(+)||PdH_x/Cu(−) electrode configuration at different E_{cell}. Error bars stand for the standard deviation of three independent measurements.

formamide ($HCONH_2$), N_2, formate ($HCOO^-$) and C_{2+} products were detected. These comparative results unequivocally demonstrate that tandem PdH_x/Cu catalysts outperform Cu in catalytic activity. After supplementation with $^{15}NO_3^-$, the products exhibited ^{1}H NMR signals nearly identical to those of the ^{15}N-urea standard and these signals disappeared when operated at open-circuit potential (OCP) (Supplementary Fig. 12). Similarly, when $^{13}CO_2$ was supplied, the ^{13}C NMR spectrum of the products matched that of ^{13}C-urea and vanished at OCP (Supplementary Fig. 12). These results provide strong evidence that the N in urea is derived from NO_3^- in the electrolyte, while the C originates from the fed CO_2. The PdH_x/Cu catalysts also demonstrated long-term stability in urea electrosynthesis (Fig. 3c), maintaining consistent catalytic activity over an extended period of 200 h.

To systematically assess catalytic performance, we conducted a comparative analysis of key performance parameters (r_{urea}, FE_{urea}, and catalytic durability) of the PdH_x/Cu catalysts, benchmarking against state-of-the-art urea electrosynthesis catalysts reported in the literature. As illustrated in Supplementary Table 2, these catalysts exhibit high r_{urea}, FE_{urea}, and long-term stability, outperforming all recently reported representative electrocatalysts[12,37–41]. These results highlight the significant advancement achieved by the tandem PdH_x/Cu system for urea electrosynthesis.

To evaluate the practical potential of the PdH_x/Cu catalysts, we scaled up a two-electrode PdH_x/Cu(+)||PdH_x/Cu(−) flow cell system. The methanol oxidation reaction (MOR) was employed as the anodic reaction instead of the oxygen evolution reaction (OER), owing to the high MOR catalytic activity of PdH_x/Cu (Supplementary Fig. 13), the significantly lower thermodynamic potential of MOR compared to OER, and the possibility for simultaneous production of valuable chemicals such as formate[42,43]. To ensure optimal conditions for MOR, the catholyte was composed of 1.0 M KOH and 0.1 M KNO_3 and continuously purged with CO_2 at a flow rate of 20 sccm. The anolyte consisted of 1.0 M KOH and 2.0 M methanol. It is noted that the presence of methanol had a negligible effect on the reported electrode

potentials throughout the electrocatalytic measurements (Supplementary Fig. 14). Using this optimized system (Supplementary Fig. 15), we achieved the highest FE_{urea} of 66.6 ± 1.3% and $FE_{formate}$ of 88.6 ± 1.4% for formate under cell voltages (E_{cell}) ranging from 2.2 to 2.8 V (Fig. 3d). Remarkably, the electrolyzer demonstrated long-term stability over 200 hours of continuous operation (Fig. 3e), yielding a urea production rate of 470.5 ± 30.1 mmol g_{cat}^{-1} h^{-1} (see ^{1}H-NMR quantification details in Supplementary Fig. 16) and a formate production rate of 2850.1 ± 51.1 mmol g_{cat}^{-1} h^{-1}. The urea quantification through spectrophotometric methods further confirmed the obtained urea production performance (Supplementary Fig. 17). To the best of our knowledge, this urea production efficiency is comparable to the best results reported to date (Supplementary Table 2).

After 200 hours of continuous operation, comprehensive post-mortem characterizations of the cathodic PdH_x/Cu catalysts were performed using XRD, TEM, XPS, FT-IR, and ^{1}H ssNMR (Supplementary Fig. 18). The analyses revealed no detectable structural or compositional changes, demonstrating long-term catalyst durability during cathodic urea electrosynthesis. In contrast, characterizations of the anodic PdH_x/Cu catalysts through XRD, FT-IR, ^{1}H ssNMR, XPS, and Raman spectroscopy showed complete lattice H* de-intercalation from PdH_x and concomitant surface oxidation of Cu during methanol electrooxidation (Supplementary Fig. 19). This transformation led to the in situ formation of catalytically active and stable Pd/CuO_x species, which maintained long-term activity for the anodic reaction–a phenomenon consistent with previous reports[44–46]. Importantly, ICP-MS analysis of the post-reaction electrolyte revealed minimal metal leaching, with total Pd and Cu concentrations measured at 2.8 ppm (Supplementary Fig. 20). This corresponds to a catalyst weight loss of only 0.42 wt.%, effectively ruling out catalyst dissolution as a significant degradation pathway. Throughout the 200-hour electrosynthesis, no detectable crossover of NO_3^- or $HCOO^-$ from the catholyte to the anolyte through the anion-exchange membrane (AEM) was observed (Supplementary Figs. 21, 22). SEM and atomic force microscopy images of the AEM before and after 200 h of continuous electrolysis through our two-electrode flow cell system revealed no significant changes in the morphology of AEM (Supplementary Fig. 23), confirming its structural stability throughout the electrosynthesis. Owing to the hydrophobic treatment of the carbon cloth gas diffusion electrode (GDE), no cathode flooding occurred throughout the 200-hour electrosynthesis period (Supplementary Fig. 24). Correspondingly, the dissolution of CO_2 into the electrolyte was significantly suppressed, which maintained a nearly constant electrolyte pH and effectively prevented salt precipitation throughout the 200-hour electrosynthesis process (Supplementary Figs. 25, 26). These findings underscore the potential robustness of the flow cell reactor based on the PdH_x/Cu(+)||PdH_x/Cu(−) configuration for practical applications. While the reported results demonstrate promising potential, both the efficiency and operational stability of the current system remain below the threshold required for practical application. As a result, challenges such as ion crossover through the AEM, membrane stability, electrode flooding, pH variation, and salt precipitation did not pose immediate concerns under the present experimental conditions. Nevertheless, these issues are expected to become critically important as the technology progresses toward real-world implementation and therefore warrant further investigation.

We then performed a preliminary economic assessment of the system's potential profitability using established models from prior researches[25,47]. The analysis incorporated both the total cost of urea electrosynthesis and the net profit from formate co-production (see Supplementary Note 1 for full methodology). The cost estimation for urea synthesis included capital investment, balance of plant, installation, maintenance, raw materials, electricity consumption, and product purification, evaluated over cell voltages (E_{cell}) ranging from 2.2 to 2.8 V. At an electricity price of US$0.01 kWh^{-1} (reflecting current rates in the Middle East), the estimated production costs slightly exceeded the current market price of urea (~US$650 per ton)[48], with a minimum achievable cost of US$935.7 per ton (Fig. 3f and Supplementary Table 3). Notably, the co-production of formate yielded net profits between US$3029.4 and US$3561.5 per ton of urea produced—calculated as formate revenue minus methanol consumption costs (Fig. 3g and Supplementary Table 4)—thereby rendering the overall process economically viable.

We then performed the preliminary evaluation of the carbon footprint for our co-production system, accounting for the fate of biogenic carbon (see details in Supplementary Note 2). When generated urea is applied as a fertilizer in agriculture—where CO_2 is ultimately released during end use—the electrochemical pathway yields life-cycle emissions of 0.923 kg CO_2 per kg of urea, significantly lower than the 1.8 kg CO_2 per kg of urea from the conventional production route[12]. These results highlight the strong potential of the PdH_x/Cu-based flow electrolyzer system for industrial-scale implementation, offering a sustainable and profitable approach for urea synthesis.

Catalytic contribution identification

The enhanced performance of PdH_x/Cu in comparison to that of Cu can be attributed to the following factors: (i) PdH_x/Cu exhibits increased active sites owing to morphological change; (ii) the PdH_x itself demonstrates high catalytic activity for urea electrosynthesis; (iii) the Cu itself serves as the primary contributor due to the electronic metal-support interaction; (iv) the interfacial PdH_x–Cu sites show pronounced catalytic synergy for urea generation; and (v) effective CO* and H* spillover promotes C-N intermediate formation and protonation for tandem urea electrosynthesis.

To determine whether the improved urea electrosynthesis activity of PdH_x/Cu originates from an increase in catalytic sites, we compared the physical surface areas of PdH_x/Cu and pure Cu using double-layer capacitance (C_{dl}) measurements derived from CV. As shown in Supplementary Fig. 27, the nearly identical C_{dl} values (82.6 mF vs. 84.4 mF) indicate comparable physical surface areas between the two catalysts. This similarity can be attributed to the low weight loading and small size (~ 3.81 nm) of the PdH_x nanoparticles, which contribute little additional surface area, combined with the partial blockage of Cu sites during deposition that may even result in a net reduction. These findings rule out the possibility that increased physical surface area is responsible for the enhanced activity. As shown in Supplementary Fig. 28, PdH_x/Cu (53.0 m^2 g^{-1}) and Cu (51.7 m^2 g^{-1}) showed the close Brunauer–Emmett–Teller (BET) surface areas, again confirming the above fact[49]. Control experiments using PdH_x nanoparticles (~ 3.70 nm) on reduced graphene oxide (PdH_x/rGO, Supplementary Fig. 29) showed significantly lower urea electrosynthesis activity (Supplementary Fig. 30), indicating the PdH_x itself is not the primary active component. We then probed whether Cu itself dominates the catalysis by selectively poisoning PdH_x with triphenylphosphine (PPh_3)[50,51]. If Cu itself were the main active phase, the activity should remain largely unaffected. Instead, a sharp decline in urea production was observed (Supplementary Fig. 31), demonstrating that the enhanced performance does not result from independent contributions from either component.

The catalytic role of interfacial sites might also dominate the urea electrosynthesis performance of PdH_x/Cu. If this were the case, a positive linear correlation should be observed among PdH_x loading, the density of PdH_x–Cu interfacial sites, and urea formation activity (Supplementary Fig. 32). To test this hypothesis, we investigated the relationship between PdH_x loading and r_{urea} (Supplementary Figs. 33, 34), with particular emphasis on low loading levels to minimize interference from particle aggregation. Interestingly, r_{urea} reached a saturation point at a PdH_x loading of 7.0 wt.%, indicating that the capacity of the Cu domains to accommodate spillovered H* (H_{Sp}*) and CO* (CO_{Sp}*) species was likely maximized at this level. These results

clearly demonstrate that the enhanced urea electrosynthesis performance of PdH_x/Cu is not primarily attributable to the PdH_x–Cu interfacial sites. After ruling out the above factors (i–iv), the improvement is most plausibly attributed to a tandem mechanism involving CO* and H* spillover.

Experimental evidence for CO* spillover

To establish conclusive evidence for CO* spillover and identify its role, we systematically designed and carried control experiments. We first performed CO temperature-programmed desorption (CO-TPD) measurements for PdH_x/rGO, Cu and PdH_x/Cu (Supplementary Fig. 35). PdH_x displayed a TPD peak at ~ 509 °C, corresponding to CO* desorption from Pd[25], whereas Cu delivered a TPD peak at ~ 160 °C, corresponding to CO* desorption from Cu[52]. Comparatively, PdH_x/Cu presented a similar CO* desorption peak to that of PdH_x (513 °C) and a sharply increased CO* desorption peak compared to that of bare Cu (165 °C), revealing the strong probability for the occurrence of CO* spillover from PdH_x to Cu in PdH_x/Cu during urea electrosynthesis. In situ differential electrochemical mass spectrometry (DEMS) was employed to monitor the $m/z = 28$ signal to investigate CO* generation behavior on PdH_x/rGO, Cu, and PdH_x/Cu catalysts during reaction in 0.2 M $KHCO_3$ electrolyte fed with CO_2 (Fig. 4a). The weak CO* signal on Cu indicates its low CO* coverage, consistent with previous reports[53]. In contrast, the exponentially enhanced CO* signal of PdH_x/Cu – PdH_x/rGO demonstrated a substantial increase in CO* coverage on the Cu component, providing direct evidence for CO* spillover from PdH_x to Cu as an additional CO* supply pathway on Cu. Further validation was obtained by PPh_3 treatment, which selectively blocked PdH_x-to-Cu CO* transfer[50,51], resulting in near-complete suppression of the CO* signal. CO-stripping cyclic voltammetry (CV) was performed on PdH_x/rGO, PdH_x/Cu, and Cu catalysts in 0.2 M $KHCO_3$ electrolyte to investigate CO* oxidation behavior (Fig. 4b). PdH_x/rGO exhibited a CO* oxidation peak at ~ 0.89 V vs. RHE, consistent with reported Pd-based catalysts[35], while Cu showed a peak at ~ 0.52 V vs. RHE, in agreement with literature[28]. Notably, the CO* oxidation peak intensity at ~ 0.52 V vs. RHE was significantly enhanced for PdH_x/Cu compared to Cu, demonstrating efficient CO* spillover from PdH_x to Cu. This conclusion was further supported by the sharp decrease in these CO* oxidation peaks at ~ 0.89 and ~ 0.52 V vs. RHE after PPh_3 treatment, which blocked the PdH_x and inhibited PdH_x-to-Cu CO* spillover[50,51]. These results provide clear clues for active CO* spillover from PdH_x to Cu in PdH_x/Cu.

To obtain direct evidence, in situ attenuated total reflectance-surface-enhanced infrared absorption spectroscopy (ATR-SEIRAS) was employed to monitor the reaction intermediates on PdH_x/rGO, PdH_x/Cu, and Cu catalysts during the reaction in 0.2 M $KHCO_3$ electrolyte (Fig. 4c–e). When only CO_2 was introduced, PdH_x/rGO exhibited a typical peak corresponding to CO* vertically adsorbed on the Pd-Pd bridge sites (PdH_x–CO_{bridge}, 1958 cm^{-1})[54], which emerged at − 0.4 V vs. RHE and increased rapidly with negative potential shift (Supplementary Fig. 36). This observation confirms the facile potential-dependent electrochemical reduction of CO_2 to CO* on PdH_x. In contrast, Cu catalysts displayed only a weak peak for CO* adsorbed on atop Cu sites (Cu–CO_{atop}, 2076 cm^{-1})[54] within the same window (Fig. 4c), indicating sluggish CO_2-to-CO* conversion. Notably, in the PdH_x/Cu system, the PdH_x–CO_{bridge} peak also showed significant potential-dependent

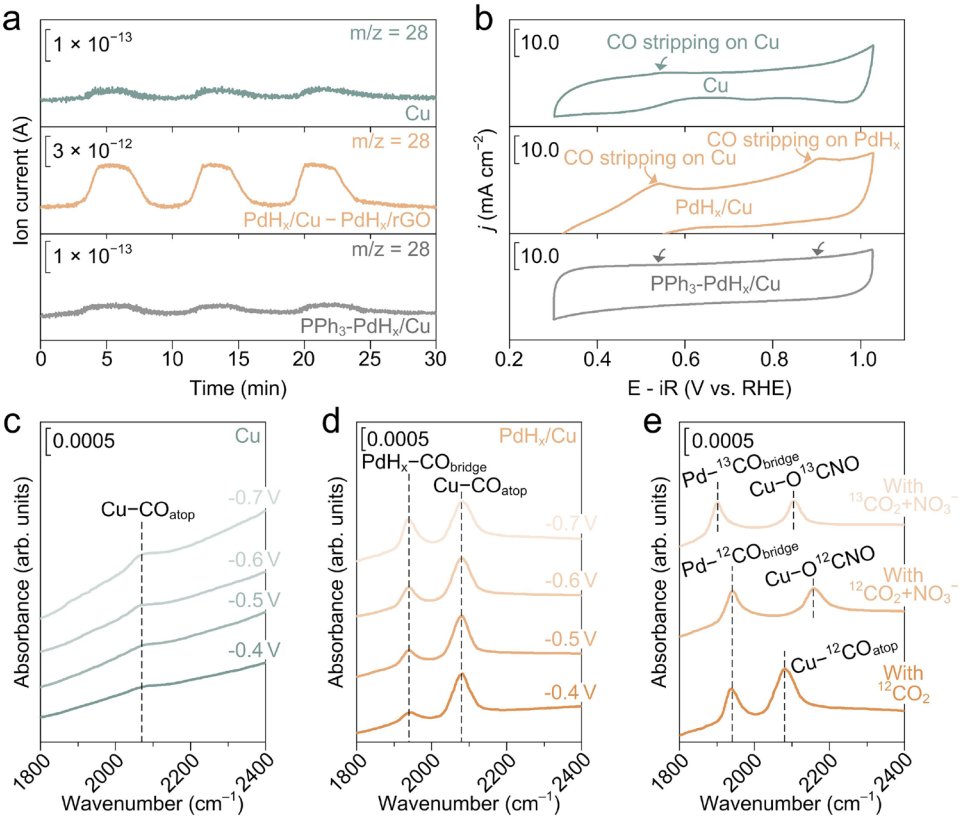

Fig. 4 | Experimental evidence for CO* spillover. a In situ DEMS investigations of various model catalysts during urea electrosynthesis without NO_3^- feeding at − 0.7 V vs. RHE. The cyan curve represents the DEMS signal of Cu. The blue curve represents the difference in the DEMS signals of PdH_x/Cu and PdH_x/rGO. The gray curve represents the DEMS signal of PPh_3-treated PdH_x/Cu. The presented ion current data represent raw signals without any post-treatment. **b** CO-stripping CVs of Cu, PdH_x/Cu and PPh_3-treated PdH_x/Cu in 0.2 M $KHCO_3$ electrolyte at a scan rate of 20 mV s^{-1}. CO(g) was pre-adsorbed from the CO-saturated electrolyte at − 0.1 V vs. RHE for 2 min. In situ ATR-SEIRAS spectra for the (**c**) Cu and (**d**) PdH_x/Cu catalysts during reaction at the potential range of − 0.4 to − 0.7 V vs. RHE in $KHCO_3$ electrolyte only fed with CO_2. **e** In situ ATR-SEIRAS spectra for the PdH_x/Cu catalysts at − 0.7 V vs. RHE in $KHCO_3$ electrolyte with different feedings.

enhancement, reaffirming efficient CO* generation on PdH_x (Fig. 4d). Strikingly, a much more pronounced Cu−CO_{atop} signal was observed even at minimal overpotentials, providing direct spectroscopic evidence for rapid CO* spillover from PdH_x to Cu.

When CO_2 and NO_3^- were co-fed, the prominent Cu−CO_{atop} peak disappeared, while a new characteristic peak corresponding to OCNO* adsorbed on Cu (Cu−OCNO) emerged at 2151 cm^{-1} (Fig. 4e)[17]. Subsequent isotopic switching from ^{12}CO to ^{13}CO in the feed resulted in the disappearance of both PdH_x–$^{12}CO_{bridge}$ and Cu−O^{12}CNO peaks, with concomitant appearance of redshifted peaks at 1905 cm^{-1} and 2110 cm^{-1}, respectively. The measured frequency shifts between the original and newly formed peaks showed excellent agreement with the expected $^{12}C/^{13}C$ isotopic shift values[55–57], confirming that the new peaks should be assigned to PdH_x–$^{13}CO_{bridge}$ and Cu−O^{13}CNO. These findings strongly confirm that CO* adsorbed on Cu originates exclusively from PdH_x via spillover, and the spillovered CO_{Sp}* actively participates in the first C-N coupling to form OCNO*. Identical spectral results were obtained from the cathodic PdH_x/Cu catalysts in the PdH_x/Cu(+)||PdH_x/Cu(−) flow cell system with 1.0 M KOH electrolyte (Supplementary Fig. 37), thereby confirming the effective operation of the CO* spillover mechanism for urea electrosynthesis in this two-electrode system.

Experimentalevidence for H* spillover

To investigate the occurrence and efficiency of H* spillover, in situ characterizations were employed to monitor H* species on the catalyst surface during the reaction. Electrochemical impedance spectroscopy (EIS) was employed to quantify the amount of H* on Cu in the PdH_x/Cu system (Supplementary Fig. 38). The EIS spectra, exhibiting two semicircles, were fitted using a dual-parallel equivalent circuit model (inset, Supplementary Fig. 38)[58]; the corresponding fitted parameters are summarized in Supplementary Table 5. The solution resistance (R_s) showed minor variations due to molecular fluctuations in the electrolyte. The first parallel element (T and R_1) corresponds to the charge-transfer kinetics of urea electrosynthesis[59]. The consistently low R_1 values across all catalysts indicate high conductivity and rapid charge-transfer capability. The second parallel element (C and R_2) characterizes H* adsorption on the catalyst surface, with R_2 and C representing the adsorption resistance and pseudocapacitance, respectively[58]. The H* adsorption charge (Q) was determined by integrating the H* adsorption capacitance (C) as a function of potential (η) derived from Nyquist plots (Fig. 5a)[60]. Control experiments were performed using bare Cu and PdH_x/rGO. Comparative analysis revealed a 6.2-fold increase in the differential H* adsorption charge (Q[PdH_x/Cu] − Q[PdH_x/rGO] = 3131 μC) relative to that of bare Cu (Q[Cu] = 502 μC), demonstrating a significant enhancement in H* generation on the Cu surface of the PdH_x/Cu system. These results provide direct evidence for efficient PdH_x-to-Cu H* spillover, which ensures a substantial H* supply on Cu.

Further investigation into the hydrogen adsorption kinetics on Cu and PdH_x/Cu during the reaction was conducted via Tafel analysis of log R_2 versus applied potential (Supplementary Fig. 39)[59], derived from EIS data (Supplementary Fig. 38 and Table 5). The Cu exhibited showed a large EIS-derived Tafel slope (136.5 mV dec^{-1}), indicative of its limited H* adsorption kinetics. In contrast, PdH_x/Cu showcased a much lower EIS-derived Tafel slope (90.1 mV dec^{-1}). This finding revealed that the intrinsic kinetic bottleneck of H* adsorption on the Cu side was overcome with sufficient PdH_x-to-Cu hydrogen spillover functioning as a

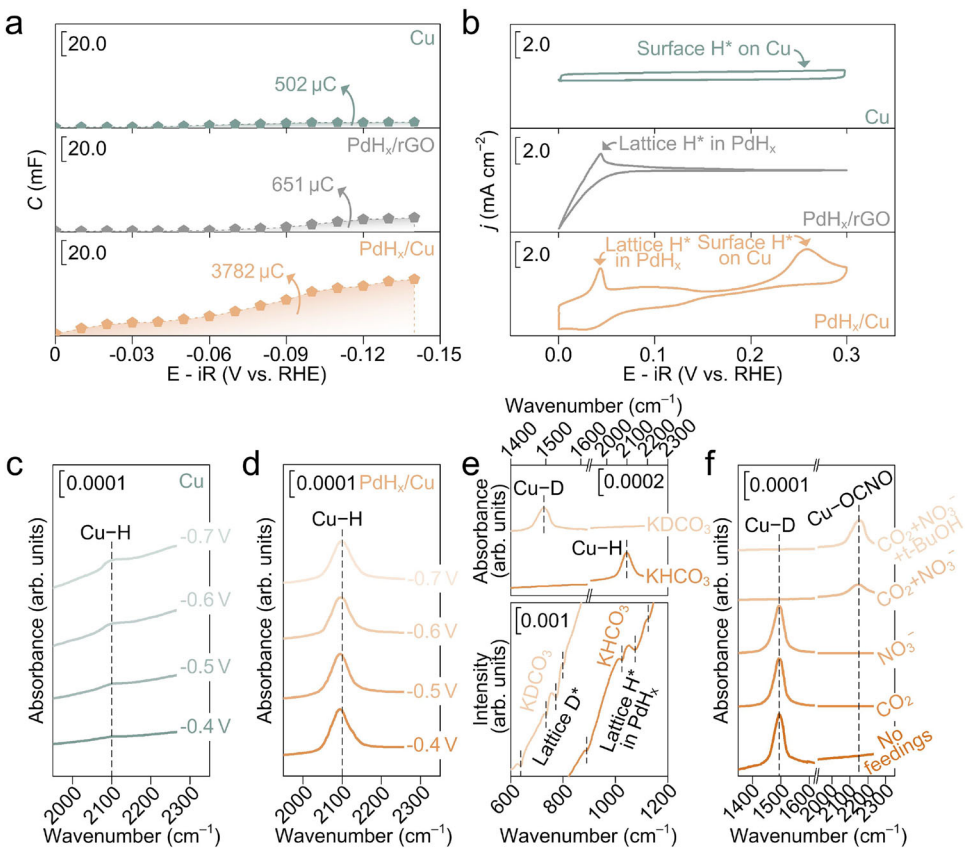

Fig. 5 | Experimental evidence for H* spillover. a Plots of C vs. η of the Cu, PdH_x/rGO and PdH_x/Cu catalysts. **b** CVs of the Cu, PdH_x/rGO and PdH_x/Cu catalysts in 0.2 M $KHCO_3$ electrolyte at a scan rate of 20 mV s^{-1}. In situ ATR-SEIRAS spectra for the (**c**) Cu and (**d**) PdH_x/Cu catalysts during reaction at the potential range of − 0.4 to − 0.7 V vs. RHE in $KHCO_3$ electrolyte without feeding. **e** In situ ATR-SEIRAS and FT-IR spectra for the PdH_x/Cu catalysts at − 0.7 V vs. RHE in $KHCO_3/H_2O$ or $KDCO_3/D_2O$ solution. **f** In situ ATR-SEIRAS for the PdH_x/Cu catalysts at − 0.7 V vs. RHE in $KDCO_3/D_2O$ solution with different feedings.

much faster pathway for H* supply. CV investigations were then performed on the PdH_x/rGO, PdH_x/Cu and Cu catalysts at a potential range from 0 to 0.3 V vs. RHE without the feeding of CO_2 and NO_3^- (Fig. 5b), enabling the in situ monitoring of H* during the reaction. PdH_x/rGO exhibited an oxidation CV peak at ~ 0.05 V vs. RHE, indicative of the typical desorption behavior of lattice H* in PdH_x[27]. Conversely, no CV peak was observed for Cu within this potential range, consistent with the intrinsically limited availability of adsorbed H* on the Cu surface. In comparison, PdH_x/Cu showed a similar lattice H* desorption signal at ~ 0.05 V vs. RHE, along with a sharply raised oxidation CV peak at 0.26 V vs. RHE. Previous reports and various control experiments (Supplementary Figs. 40–42) confirmed that this oxidation CV peak corresponded to the H* desorption on Cu rather than OH* or metal/hydroxide redox behavior[28,61,62]. These observations provide evidence for efficient H* spillover from PdH_x lattice to Cu surface and thus sufficient spillovered H_{Sp}* for desorption.

To demonstrate H* spillover mechanism, we conducted in situ ATR-SEIRAS measurements on PdH_x/Cu and Cu catalysts in 0.2 M $KHCO_3/H_2O$ electrolyte (Fig. 5c, d). Upon sweeping the potential from − 0.4 to − 0.7 V vs. RHE, the Cu catalyst exhibited weak vibrational signature of adsorbed H* (Cu–H, 2102 cm^{-1})[63], consistent with its inherently low hydrogen adsorption capability. In stark contrast, PdH_x/Cu displayed an intense Cu–H signal even at minimal potential, indicating a H* spillover process that facilitates rapid H* transfer from PdH_x to Cu[28]. Further mechanistic validation was achieved through isotopic exchange experiments (Fig. 5e), where replacing $KHCO_3/H_2O$ with $KDCO_3/D_2O$ resulted in the complete disappearance of the Cu–H signal and the emergence of a redshifted Cu–D signal at 1500 cm^{-1}, matching the theoretical H/D isotopic shift ratio ($1/\sqrt{2}$)[64,65]. Complementary in situ FT-IR transmission spectra confirmed the concurrent depletion of the lattice Pd–H signals (893, 1025, 1079 and 1130 cm^{-1}) in PdH_x and the formation of lattice Pd–D signals (638, 732, 771 and 807 cm^{-1}), directly linking the H_{Sp}* to the dynamic (de)intercalation of lattice H* in PdH_x[24]. These spectroscopic observations provide unequivocal evidence for a lattice H* spillover mechanism, wherein PdH_x acts as an H* reservoir, supplying lattice H* to Cu via a (de)intercalation cycle and subsequent spillover.

Following the introduction of CO_2 or NO_3^-, Cu–D vibrational signal remained largely unaltered (Fig. 5f), indicating that the spillovered D* (or H* under non-isotopic conditions) on Cu less participates in the electroreduction of CO_2 or NO_3^- during urea electrosynthesis. Notably, when both CO_2 and NO_3^- were introduced simultaneously, Cu–D signal rapidly diminished and Cu–OCNO signal came into being. Further mechanistic insight was gained by adding the D* trap tertiary butanol (t-BuOH) to the electrolyte[66], which resulted in a marked increase in the Cu–OCNO signal. These observations provide compelling evidence that the H_{Sp}* actively facilitates the protonation of key C-N coupling intermediates (e.g., OCNO*). The cathodic PdH_x/Cu catalysts in the PdH_x/Cu(+)||PdH_x/Cu(−) flow cell system exhibited identical spectral results in 1.0 M KOH/H_2O electrolyte (Supplementary Fig. 43). This consistency provides direct evidence for the efficacy of the H* spillover mechanism on these catalysts during urea electrosynthesis within this two-electrode configuration. Collectively, these findings confirm the occurrence of a tandem urea electrosynthesis mechanism over PdH_x/Cu as initially hypothesized, in which surface CO* and lattice H* spillover from PdH_x-to-Cu drive first C-N coupling and protonation of the resulting C-N intermediates during urea electrosynthesis.

Mechanistic insights

To elucidate the role of the tandem mechanism in urea electrosynthesis, we first experimentally identified the reaction pathway for urea electrosynthesis over the Cu and PdH_x/Cu catalysts through online DEMS. When co-fed with CO_2 and NO_3^-, signals at m/z = 58 and 44 were detected (Supplementary Fig. 44). Control experiments with only CO_2 or only NO_3^- showed no significant signals at these m/z values (Supplementary Fig. 45), confirming that these fragments do not originate from the electroreduction of CO_2 or NO_3^- alone. Therefore, the signals at m/z = 58 and 44 can be attributed to the key OCNO* and $OCNH_2$* intermediates, respectively, during urea electrosynthesis. Taken together, the following reaction pathways were identified: (i) first C-N coupling (CO* + NO* → OCNO*) and protonation to $OCNH_2$*; (ii) second C-N coupling ($OCNH_2$* + NO* → OCNO*) and protonation to urea[16]. Accordingly, we examined the free energy profiles of key reaction steps on the Cu model. The CO_2 reduction pathway (CO_2(g)-to-CO*) exhibits a high barrier of 0.46 eV in the step of CO_2(g) → COOH* (Fig. 6a), making CO* formation energetically unfavorable. In contrast, NO_3^- reduction (NO_3^-(g)-to-NO*) is energetically favorable (Fig. 6b). However, the first C-N coupling (CO* + NO* → OCNO*) is severely limited by both the scarcity of CO* intermediates and a formidable coupling barrier of 0.70 eV (Fig. 6c). In addition, Cu model demonstrates stagnant water dissociation process (Supplementary Fig. 46), resulting in an insufficient supply of H*. Consequently, the protonation of the resulting OCNO* through the proton-coupled electron transfer (PCET) pathway (OCNO* → OCNOH* → OCN* → $OCNH_2$*) face a notably high barrier of 0.70 eV at the OCN* → OCNH* step (Fig. 6c). These combined limitations in first C-N intermediate formation and protonation explain the experimentally observed negligible urea production on the Cu catalysts.

Accordingly, the free energy profiles for urea electrosynthesis were computed on the PdH_x/Cu model (see Methods for calculation details and model construction). On PdH_x/Cu surface, the PdH_x domain enables energetically favorable CO_2 reduction, producing vertically oriented CO* at surface site-1 ($CO_{Sf\text{-}1}$*, Fig. 6d). Notably, a surface CO* spillover channel from PdH_x ($CO_{Sf\text{-}1}$*) → interface ($CO_{Sf\text{-}2}$* and $CO_{Sf\text{-}3}$*) → Cu (CO_{Sp}*) with gradually weakened CO* adsorption exists (Fig. 6e). Through this channel, the PdH_x-generated CO* can efficiently migrate to Cu sites with a low barrier of 0.26 eV. Concurrently, the Cu domain efficiently catalyzes NO_3^- reduction, generating abundant NO* intermediates (Fig. 6f). The spatial proximity of CO_{Sp}* (from PdH_x surface to Cu) and NO* (generated on Cu) enables first C-N coupling (CO_{Sp}* + NO* → OCNO*) with a significantly reduced barrier of 0.30 eV (Fig. 6g). The PdH_x further serves as an efficient H* reservoir: (i) lattice H* (H_{L1}* and H_{L2}*) undergoes facile de-intercalation and spillover to Cu sites, and (ii) protons from the electrolyte spontaneously intercalate into the PdH_x lattice, maintaining a sustainable H* supply for Cu domain (Fig. 6h). Given the high energy barriers associated with H_{Sp}*-mediated CO_2 or NO_3^- electroreduction (Supplementary Figs. 47, 48), the resulting OCNO* can be readily protonated by H_{Sp}* to form $OCNH_2$* via a series of steps (OCNO* + H_{Sp}* → OCNOH* → OCNOH* + H_{Sp}* → OCN* → OCN* + H_{Sp}* → OCNH* → OCNH* + H_{Sp}* → $OCNH_2$*). With a continuous supply of H_{Sp}* (from the PdH_x lattice to Cu) and NO* (generated on Cu), the subsequent almost barrierless second C-N coupling (NO* + $OCNH_2$* → $ONOCNH_2$*) and successive protonation steps leading to urea formation ($ONOCNH_2$* + H_{Sp}* → $HONOCNH_2$* → $HONOCNH_2$* + H_{Sp}* → $NOCNH_2$* → $NOCNH_2$* + H_{Sp}* → $HNOCNH_2$* → $HNOCNH_2$* + H_{Sp}* → H_2NOCNH_2(g)) proceed efficiently, as illustrated in Fig. 6g. Consequently, PdH_x/Cu establishes an energetically optimized tandem pathway for urea electrosynthesis, where first coupling between CO_{Sp}* and NO* onto Cu emerges as the rate-determining step (RDS) with a much lower barrier of 0.30 eV compared to that of the Cu counter (0.70 eV), accounting for the significantly enhanced r_{urea}.

In addition, the competing reaction pathways over both PdH_x and Cu domains were investigated. The side reactions of CO_2 reduction to CO(g) and NO_3^- reduction to NH_3(g) exhibit high energy barriers (minimum 0.56 eV; see Fig. 6d, f, and Supplementary Figs. 49, 50), which effectively suppress the formation of CO(g) and NH_3(g) byproducts. The direct coupling between CO* and NO* intermediates on the PdH_x domains of the PdH_x/Cu model was also found to face a substantial barrier of 1.42 eV in the CO* + NO* → OCNO* step

https://doi.org/10.1038/s41467-026-69307-1

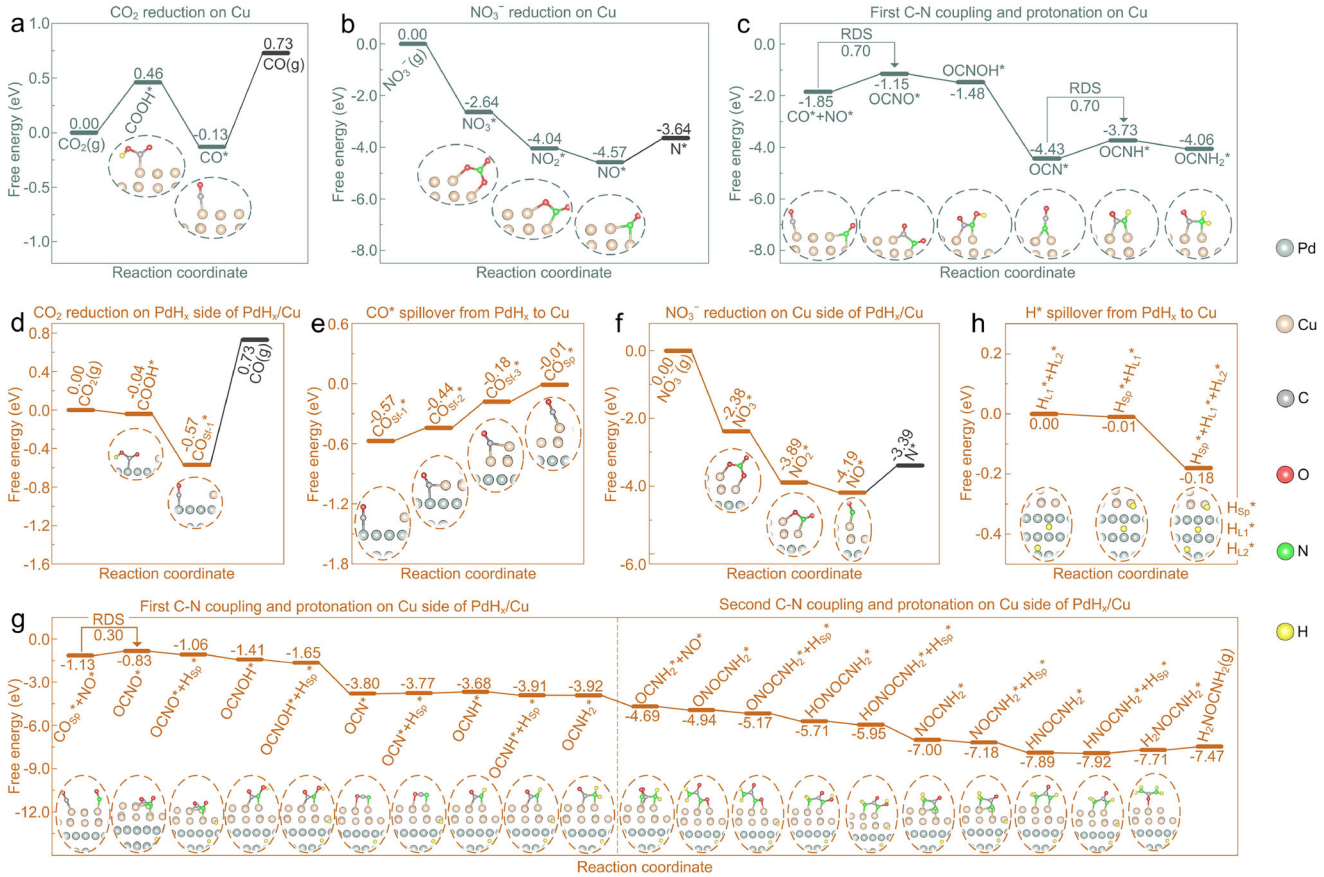

Fig. 6 | Mechanistic insights. a Calculated free energy diagrams of the CO_2 reduction on Cu model. **b** Calculated free energy diagrams of the NO_3^- reduction on Cu model. **c** Calculated free energy diagrams of C-N coupling and protonation on Cu model. **d)** Calculated free energy diagrams of the CO_2 reduction on the PdH_x side of the PdH_x/Cu model. **e** Calculated free energy diagrams of CO* spillover from PdH_x surface to Cu surface on PdH_x/Cu model. **f** Calculated free energy diagrams of the NO_3^- reduction on the Cu side of PdH_x/Cu model. **g** Calculated free energy diagrams of C-N coupling and protonation on the Cu side of PdH_x/Cu model. **h** Calculated free energy diagrams of H* spillover from PdH_x lattice to Cu surface on PdH_x/Cu model.

(Supplementary Fig. 51), ruling out this pathway. Further calculations of water dissociation energies on PdH_x, the PdH_x–Cu interface, and Cu domains revealed high barriers of 0.54 eV, 0.58 eV, and 0.40 eV, respectively (Supplementary Figs. 52–54), indicating that HER is also strongly inhibited. Similarly, the competing HER pathway via the coupling of H_{Sp}* species and protons from the electrolyte on the Cu domains of the PdH_x/Cu model showed a high barrier of 0.42 eV in the $H^* + H^+ + e^- \rightarrow H_2^*$ step (Supplementary Fig. 55), further excluding this possibility. These collective mechanistic insights rationalize the observed high FE_{urea} over the PdH_x/Cu catalysts. It is important to note that these DFT calculations were performed on idealized models under standard conditions. Accordingly, key practical aspects such as explicit solvent effects and catalyst dynamics are thus not fully described in our current computational setup.

To experimentally support the theoretical results, a series of controlled experiments were systematically conducted. The kinetic isotope effect (KIE) was investigated by comparing r_{urea} at − 0.7 V vs. RHE using $^{12}CO_2$ and $^{13}CO_2$ as reactants (Supplementary Fig. 56). The measured KIE value of 1.61 strongly indicated that surface CO* spillover or OCNO* formation constitutes the RDS in the urea electrosynthesis process. Considering that the in situ Fourier transform infrared spectroscopy results for PdH_x/Cu showed more significant characteristic peaks as well as increased coverage of adsorbed NO* species with an increase in the NO_3^- concentration during urea electrosynthesis (Supplementary Fig. 57), we further explored the urea electrosynthesis performance of PdH_x/Cu with different NO_3^- concentrations. The observed significant enhancement in r_{urea} with increasing NO_3^- concentrations (Supplementary Fig. 58) provides compelling experimental evidence that the C-N coupling constituted the RDS. This conclusion is supported by the premise that more NO_3^- (or higher coverage of NO* species) would promote more frequent effective collisions with CO*, thereby accelerating the reaction kinetics if C-N coupling is indeed the RDS[67]. To gain deeper mechanistic insights, we determined the apparent activation energy (E_a) for urea electrosynthesis by analyzing the temperature dependence of r_{urea} at − 0.7 V vs. RHE (Supplementary Fig. 59). The significantly lower E_a observed for PdH_x/Cu compared to bare Cu (25.4 kJ mol^{-1} vs. 36.1 kJ mol^{-1}) provides direct experimental evidence for the accelerated reaction kinetics enabled by CO* and H* spillover effects. To further verify this hypothesis, we measured the E_a of PPh_3-treated PdH_x/Cu, which selectively poisons the PdH_x domain and suppresses spillover processes. The resulting E_a (43.5 kJ mol^{-1}) was substantially higher than that of the untreated catalyst (Supplementary Fig. 60), reinforcing the critical role of CO* and H* spillover in facilitating urea electrosynthesis. These experimental observations—spanning KIE measurements, concentration-dependent kinetics, and E_a analyses—exhibit excellent agreement with our DFT calculations.

Discussion

In summary, we reported a dual spillover mechanism of CO* and H* to initiate an improved tandem urea electrosynthesis pathway over PdH_x/Cu, where PdH_x and Cu enabled efficient CO_2-to-CO* and NO_3^--to-NO*

conversions, followed by rapid CO* spillover from PdH_x surface to Cu for promoted C-N coupling and simultaneous H* spillover from PdH_x lattice to Cu for facilitated C-N intermediate protonation. Consequently, these catalysts showed a high performance for urea electrosynthesis. These unique findings regarding CO* and H* spillover will broaden concepts for tandem catalyst design and provide new considerations for industrial urea electrosynthesis.

Methods

Synthesis of PdH_x/Cu

Based on previously established methodologies[32], the synthesis was carried out as follows. Initially, 50 mg of palladium acetylacetonate (99.9%, Macklin), 160 mg of polyvinylpyrrolidone (99.9%, Macklin), and 185 mg of cetyltrimethylammonium bromide (99.9%, Macklin) were dissolved in a mixed solvent consisting of 10 mL of N,N-dimethylformamide (99.9%, Macklin) and 2 mL of water under magnetic stirring. The resulting homogeneous yellow solution was transferred to a Schlenk flask, charged with CO gas, and immersed in a water bath at 60 °C for 12 h. After this, 10 mL of formaldehyde (37.0 wt.%, Macklin) solution was added, and the mixture was transferred to a 50 mL Teflon-lined stainless steel autoclave and heated at 160 °C for 4 h. The resulting PdH_x was collected by centrifugation at a centrifugation speed of approximately 18,900 × *g* for 10 min and washed three times with ethanol. For the preparation of PdH_x/Cu catalysts, 200 mg of $Cu(NO_3)_2{\cdot}3H_2O$ (99.9%, Energy Chemical), 200 mg of L-ascorbic acid (99.9%, Macklin), and 4.0 mg of as-synthesized PdH_x were dispersed in 30 mL of deionized water. Then, 200 mg of hexadecyltrimethylammonium bromide (99.9%, Macklin) and 200 mg of hexamethylenetetramine (99.9%, Macklin) were added to the mixture. The reaction system was sealed and heated at 80 °C for 3 h in an oil bath. The final products were isolated by centrifugation, rinsed repeatedly with distilled water and ethanol, and dried in a vacuum oven at 60 °C for 12 h to obtain the PdH_x/Cu catalysts.

Synthesis of PdH_x/rGO controls

50 mg rGO (99.9%, XFNANO) was mixed with 200 µL of the aforementioned CO-injected yellow solution (Pd content = 20 mg mL^{-1}) and 10 mL formaldehyde solution, and transferred into a 15 mL Teflon-lined stainless steel autoclave and maintained at 160 °C for 4 h. The PdH_x/rGO products were collected by centrifugation (centrifugation speed of 18,900 × *g*, 10 min) and washed three times with ethanol.

Synthesis of Cu controls

$Cu(NO_3)_2{\cdot}3H_2O$ (100 mg) and L-ascorbic acid (200 mg) were mixed with 30 mL of deionized water and stirred to form a homogeneous solution. Then, hexadecyltrimethylammonium bromide (200 mg) and hexamethylenetetramine (200 mg) were added followed by 30 min of stirring. The mixture was sealed and heated to 80 °C for 3 h in an oil bath. The resulting products were centrifuged, rinsed with distilled water and ethanol several times, and then dried in a vacuum oven at 60 °C for 12 h.

Synthesis of Pd/Cu controls

The as-prepared Cu nanosheets (50 mg) were suspended in 47 ml of distilled water, and then 70 µL $PdCl_3$ (99.9%, Macklin) solution (Pd content = 5 mg mL^{-1}) was added. Subsequently, 3 mL of the freshly prepared $NaBH_4$ (99.9%, Macklin) aqueous solution (containing 95 mg $NaBH_4$) was quickly added under vigorous stirring. After 3 h reaction under stirring, the products were collected through centrifuging, washed with water/ethanol thoroughly and then dried at 60 °C for 12 h under vacuum to obtain the Pd/Cu.

Characterization

A Bruker D8 Focus Diffraction System was employed to record the XRD patterns of the products using a Cu Kα source (λ = 0.154 nm). TEM and EDX measurements were performed on a JEOL 2100 F TEM with an accelerating voltage of 200 kV. XPS results were recorded on a photoelectron spectrometer using Al Kα radiation as the excitation source (PHI 5000 VersaProbe). The C 1*s* spectrum at a binding energy level of 284.8 eV was used to calibrate all the peaks. The metal content of various electrodes was examined by ICP-MS (Agilent 7500CE). All samples for ICP-MS were pre-treated by aqua regia to obtain clear solutions before measurements. FT-IR spectra were recorded with a NICOLET 6700 IR spectrometer (Thermo Fisher U.S.A.). The ^1H ssNMR data were collected Bruker AVANCE III HD 400 MHz NMR spectrometer. The test was performed using an H/X dual-resonance solid probe, 4 mm ZrO_2 rotor, spinning speed of 10 kHz, resonance frequency of 400.13 MHz, acquisition time of 2.5 µs, and a recycle delay of 3 s. Raman spectra data collected alpha 300 R. The test was performed 532 nm TEM00 laser, with the laser intensity set at 50% and the exposure time set at 15 s.

CO-TPD measurements

CO-TPD experiments were performed on a Chembet Pulsar instrument (Quantachrome Instruments, USA). A 50 mg sample was pretreated at 100 K for 3 h in a CO atmosphere and cleaned with an Ar gas flow for 30 min to remove the weakly adsorbed CO. The TPD process was performed by heating the sample from 0 to 700 °C at a ramp rate of 2.5 °C min^{-1} under an Ar atmosphere.

In situ IR

In situ IR experiments were carried out by a NICOLET 6700 IR spectrometer (Thermo Fisher U.S.A.) equipped with a chemically deposited ultra-thin Au film as working electrode for IR-signal enhancement (Supplementary Fig. 61). The obtained various catalysts were directly loaded on the working electrode, while Ag/AgCl and Pt foil served as reference electrode and counter electrode, respectively. It should be noted that the Ar gas was continuously bubbled into the electrolyte before and during the test. In situ IR signals were recorded when the electrodes were under potentiostatic tests.

Online DEMS measurements

Online DEMS measurements were conducted using an electrochemical cell coupled to a mass spectrometer (QAS 100, Linglu Instruments). Product detection was enabled by a porous PTFE membrane (Porosity ≥ 50%, pore size ≤ 20 nm; PF-002HS, Hangzhou Cobetter Filtration Equipment) coated on the back side of the working electrode (Supplementary Fig. 62). The experiments employed a 50 mL Ar-saturated 0.2 M $KHCO_3$ electrolyte with different chemical feedstocks. A constant cathodic potential of − 0.7 V vs. RHE was applied during reaction, and the corresponding mass signals of various intermediates for the catalysts were monitored at different m/z ionic signals.

Electrochemical measurements

The catalyst ink was prepared by dispersing 1 mg of catalyst in a mixture of isopropanol (200 µL) and Nafion (40 µL, 5.0%, Macklin). The inclusion of Nafion serves two key purposes: (i) it acts as a binder, securing catalyst particles to GDE and preventing delamination during prolonged operation[68]; and (ii) it facilitates efficient proton transport between active sites due to its high proton conductivity[69].

A CHI 760E workstation (CH Instruments, Inc., Shanghai) over two self-designed flow cells with electrode window areas of 1.0 cm^2 and 9.0 cm^2 was used for the measurements. For the three-electrode system, the catalyst ink was uniformly deposited onto a carbon paper gas diffusion electrode (GDE, Suzhou Sinero Technology Co., Ltd) using an ultrasonic spray coater (Sono-Tek ExactaCoat system) to achieve a catalyst loading of 0.4 mg cm^{-2}. The synthesized GDE, Ag/AgCl, and nickel foam served as the working, reference, and counter electrodes, respectively. The catholyte and anolyte were formulated by dissolving $KHCO_3$ in deionized water to form 0.2 M solutions (pH = 8.31 ± 0.02).

The catholyte (60 mL) containing 0.1 M KNO_3 is in a flow rate of 2.0 sccm and was supplied with 20.0 sccm of CO_2, and the anolyte (60 mL) is in a flow rate of 2.0 sccm. An anion exchange membrane (AEM, Fumasep FAB-PK-130) was utilized to separate the anode and cathode into different electrolytes. The gaseous products were collected from the gas bag while the liquid products were collected from the cathode electrolyte bottle. For a typical measurement, urea electrosynthesis was driven by a potentiostatic test at the given potential for 1.0 h. The on-the-fly iR-compensation mode with a compensation proportion of 95% was applied in each test through software tools. Electrochemical impedance spectroscopy (EIS) investigations were conducted on the GAMRY Reference 600 electrochemistry workstation in the frequency range of 100 kHz–0.1 Hz at various overpotentials. The potentials reported are relative to the reversible hydrogen electrode (RHE). To realize the calibration, an actual reversible hydrogen electrode (RHE) was submerged in 0.2 M $KHCO_3$ electrolyte and a reductive current density of approximately − 1.0 mA cm^{-2} was applied to generate H_2 inside the RHE. The potential of the Ag/AgCl reference electrodes was determined to be 0.610 V vs. RHE (Supplementary Fig. 63).

For the two-electrode measurements, the catalyst ink was first prepared by dispersing 4 mg of the PdH_x/Cu catalysts into a mixed solvent containing isopropanol (1000 µL) and Nafion (100 µL). For the fabrication of the catalytic electrodes, the catalyst ink was applied to a carbon paper GDE (Suzhou Sinero Technology Co., Ltd) at a loading of 0.44 mg cm^{-2} to form the cathode, and to a titanium felt GDE (Suzhou Sinero Technology Co., Ltd) at the same loading of 0.44 mg cm^{-2} to form the anode. The anode and cathode were separated by the anion exchange membrane (Fumasep FAB-PK-130). The catholyte and anolyte were formulated by dissolving KOH in deionized water to form 1.0 M solutions (pH = 13.69 ± 0.03). The catholyte (60 mL) containing 0.1 M KNO_3 is in a flow rate of 2.0 sccm and was supplied with 20.0 sccm of CO_2, and the anolyte (60 mL) and 2.0 M methanol is in a flow rate of 2.0 sccm. For a typical measurement, urea electrosynthesis was driven by a potentiostatic test at the given cell voltage for 1.0 h.

Product analysis

The following previously reported methods were employed for detection:

Urea. The urea products were analyzed with an NMR spectrometer (AVANCE III HD 400). Initially, a urea standard solution (500 µL) at different concentrations was mixed with a DMSO-d6 solution (150 µL) as an internal standard for ^{1}H NMR detection to obtain the relationship between the urea–DMSO-d6 peak area ratio and the urea concentration (Supplementary Fig. 64). 500 µL of the post-reaction electrolyte was neutralized to pH ≈ 7 and mixed with 150 µL of DMSO-d6 for ^{1}H NMR detection. Through the obtained urea–DMSO-d6 peak area ratio, the concentration of generated urea can be calculated. The urea products were also analyzed with a UV-Vis spectrometer (Beijing Purkinje GENERAL Instrument Co., Ltd, TU-1950). Initially, the color agent was prepared by dissolving $FeCl_3$ (0.2 mg), diacetylmonoxime (1.0 mg) and thiosemicarbazide (5 mg) into the mixed solution, which contained H_3PO_4 solution (15.0 M, 200 µL), H_2SO_4 (18.4 M, 600 µL) solution and deionized water (1200 µL). A series of standard urea solutions (0.5 mL) with different urea concentrations was mixed with the color agent for 30 min for UV-Vis measurements. The absorption intensity at a wavelength of 525 nm was recorded, providing the corresponding concentration-absorbance curve as shown in Supplementary Fig. 65. Then, the electrolyte was collected, diluted and mixed with the above color agent for UV-Vis detection. Through the obtained absorption intensity at 525 nm, the concentration of generated urea can be calculated.

$HCONH_2$. The $HCONH_2$ products were analyzed with an NMR spectrometer (AVANCE III HD 400). Initially, a $HCONH_2$ standard solution (500 µL) at different concentrations was mixed with a DMSO-d6 solution (150 µL) as an internal standard for ^{1}H NMR detection to obtain the relationship between the $HCONH_2$ – DMSO-d6 peak area ratio and the $HCONH_2$ concentration (Supplementary Fig. 66). 500 µL of the post-reaction electrolyte was neutralized to pH ≈ 7 and mixed with 150 µL of DMSO-d6 for ^{1}H NMR detection. Through the obtained $HCONH_2$ – DMSO-d6 peak area ratio, the concentration of generated $HCONH_2$ can be calculated.

NH_3. UV-Vis absorbance spectra were obtained to analyze the concentrations of the reactants and products of NH_3. All electrolytes were diluted to appropriate concentrations before spectrophotometric analysis. A color agent was prepared by dissolving salicylic acid (0.1 g) and sodium citrate (0.1 g) in NaOH solution (2 mL, 1.0 M) and then mixing with NaClO solution (1 mL, 0.05 M), sodium nitroferricyanide solution (0.2 mL, 1.0 wt%) and diluted electrolytes (5 mL) evenly. After standing for 30 min, the absorption intensity was recorded at a wavelength of 654 nm, and the concentration of produced NH_3 could be estimated through the concentration–absorbance curve using various standard NH_4Cl solutions, as shown in Supplementary Fig. 67.

NO_2^-. The ultraviolet-visible (UV-Vis) absorbance spectra were employed to analyze the NO_2^- products. To realize UV-Vis analysis, the color agent was prepared by dissolving p-aminobenzenesulfonamide (4 g) and N-(1-Naphthyl) ethylenediamine dihydrochloride (0.2 g) into ultrapure water (50 mL). Then, a series of standard $NaNO_2$ solutions (5 mL) with different NO_2^- concentrations was mixed with the color agent (0.1 mL) for 20 min for UV-Vis measurements. The absorption intensity at a wavelength of 540 nm was recorded, providing the corresponding concentration-absorbance curve as shown in Supplementary Fig. 68. The electrolyte (5 mL) in the cathodic chamber was diluted and mixed with the above color agent for UV-Vis detection, and through the obtained absorption intensity at 540 nm, the concentration of generated NO_2^- can be calculated.

CH_3COOH. The CH_3COOH products were analyzed via an NMR spectrometer. Initially, different concentrations of the CH_3COOH standard solution (500 µL) were mixed with a DMSO-d6 solution (150 µL) for ^{1}H NMR detection to obtain the relationship between the CH_3COOH – DMSO-d6 peak area ratio and the CH_3COOH concentration (Supplementary Fig. 69). After neutralizing the pH of post-reaction electrolyte to 7, the generated CH_3COOH in electrolyte could be estimated through this concentration–peak area curve.

$HCOO^-$. The $HCOO^-$ products were analyzed via an NMR spectrometer. Initially, different concentrations of the $HCOO^-$ standard solution (500 µL) were mixed with a DMSO-d6 solution (150 µL) for ^{1}H NMR detection to obtain the relationship between the $HCOO^-$ – DMSO-d6 peak area ratio and the $HCOO^-$ concentration (Supplementary Fig. 70). After neutralizing the pH of the post-reaction electrolyte to 7, the generated $HCOO^-$ in the electrolyte could be estimated through this concentration–peak area curve.

CO, H_2 and N_2. The generated CO, H_2 and N_2 were collected via a gas bag and analyzed via a gas chromatography instrument (North Point GC 901 A) equipped with a thermal conductivity detector and a flame ionization detector.

FE evaluation. The FE of the relevant reactions was calculated as follows:

$$FE(\%) = nFm/Q$$

where n is the electron-transfer number of relevant reactions, m is the amount of generated products, F is the Faradaic constant

(96485 C mol^{-1}), and Q is the total charge passed through the electrode.

Computational details. All spin-polarized DFT calculations were performed using the Vienna Ab-initio Simulation Package (VASP) software[70,71]. The Perdew-Burke-Ernzerhof (PBE) under the generalized gradient approximation (GGA) was used to describe exchange-correlation functional[72,73]. In the process of geometric optimization, the 400 eV is set as the plane wave cutoff energy (Supplementary Fig. 71) meanwhile the 0.03 eV/Å and 1×10^{-5} eV are set as the convergence criterion of force and energy, respectively. The dispersion corrections are applied using the Grimme's DFT-D3 method[74]. The optimized Monkhorst-Pack mesh of (1 × 2 × 1) is set for our system due to it achieves computational efficiency without compromising accuracy (Supplementary Table 6)[75]. The Gibbs free energy is corrected to the experimental temperature (298.15 K) using the VASPKIT software package[76].

High resolution TEM image of the as-prepared PdH_x/Cu catalysts (Fig. 2b) showed a Pd(111) facet for the PdH_x in PdH_x/Cu, and a Cu(111) facet for the Cu in PdH_x/Cu. To simulate the PdH_x component and its lattice H* spillover phenomenon, we firstly built a three-layer Pd slab model derived from Pd(111) with two H atoms inserted into its bulk phase similar to our previous work[24]. Then, we built a two-layer Cu cluster model originated from Cu(111) and placed the Cu cluster on the PdH_x slab surface, finally creating the PdH_x/Cu model. For comparison, the Cu cluster model was also employed. The optimized Cu cluster and PdH_x/Cu geometries are shown in Supplementary Fig. 72.

In order to determine the change of Gibbs free energy (ΔG) of each elemental step, the following equation was employed: ΔG = ΔE + ΔZPE − TΔS, where ΔE refers to the electronic energy difference directly obtained from DFT calculations, ΔZPE represents the change in zero-point energies, T denotes the temperature (T = 298.15 K), ΔS accounts for the entropy change[77].

Data availability

The authors declare that the main data supporting the findings of this study are available within the article and its Supplementary Information. Extra data are available from the corresponding authors upon request. Source data are provided in this paper.

References

1. Zhang, X. et al. Managing nitrogen for sustainable development. *Nature* **528**, 51–59 (2015).
2. Kohlhaas, Y. et al. Electrochemical urea synthesis. *Joule* **8**, 1579–1600 (2024).
3. Li, J., Zhang, Y., Kuruvinashetti, K. & Kornienko, N. Construction of C-N bonds from small-molecule precursors through heterogeneous electrocatalysis. *Nat. Rev. Chem.* **6**, 303–319 (2022).
4. Chen, C. et al. Coupling N_2 and CO_2 in H_2O to synthesize urea under ambient conditions. *Nat. Chem.* **12**, 717–724 (2020).
5. Regnier, P., Resplandy, L., Najjar, R. G. & Ciais, P. The land-to-ocean loops of the global carbon cycle. *Nature* **603**, 401–410 (2022).
6. Schulte-Uebbing, L. F., Beusen, A. H. W., Bouwman, A. F. & de Vries, W. From planetary to regional boundaries for agricultural nitrogen pollution. *Nature* **610**, 507–512 (2022).
7. Lv, C. et al. Selective electrocatalytic synthesis of urea with nitrate and carbon dioxide. *Nat. Sustain.* **4**, 868–876 (2021).
8. van Langevelde, P. H., Katsounaros, I. & Koper, M. T. M. Electrocatalytic nitrate reduction for sustainable ammonia production. *Joule* **5**, 290–294 (2021).
9. Liu, W. et al. Efficient ammonia synthesis from the air using tandem non-thermal plasma and electrocatalysis at ambient conditions. *Nat. Commun.* **15**, 3524 (2024).
10. Liu, W. et al. Full runner electrolyzer stack for industrial-current-density NO_x^--mediated ammonia synthesis from air and water. *Nat. Commun.* **16**, 5716 (2025).
11. Liang, H.-Q., Beweries, T., Francke, R. & Beller, M. Molecular catalysts for the reductive homocoupling of CO_2 towards C_{2+} compounds. *Angew. Chem. Int. Ed.* **61**, e202200723 (2022).
12. Luo, Y. et al. Selective electrochemical synthesis of urea from nitrate and CO2 via relay catalysis on hybrid catalysts. *Nat. Catal.* **6**, 939–948 (2023).
13. Zhang, X. et al. Electrocatalytic urea synthesis with 63.5 % Faradaic efficiency and 100 % N-selectivity via one-step C-N coupling. *Angew. Chem. Int. Ed.* **62**, e202305447 (2023).
14. Xu, M. et al. Kinetically matched C-N coupling toward efficient urea electrosynthesis enabled on copper single-atom alloy. *Nat. Commun.* **14**, 6994 (2023).
15. Tu, X. et al. A universal approach for sustainable urea synthesis via intermediate assembly at the electrode/electrolyte interface. *Angew. Chem. Int. Ed.* **63**, e202317087 (2024).
16. Cheng, M. et al. Rectifying heterointerface facilitated C-N coupling dynamics enables efficient urea electrosynthesis under ultralow potentials. *Angew. Chem. Int. Ed.* **64**, e202413534 (2025).
17. Wang, Y. et al. Electron deficiency is more important than conductivity in C-N coupling for electrocatalytic urea synthesis. *Angew. Chem. Int. Ed.* **63**, e202410938 (2024).
18. Song, X. et al. Urea synthesis via coelectrolysis of CO_2 and nitrate over heterostructured Cu-Bi catalysts. *J. Am. Chem. Soc.* **146**, 25813–25823 (2024).
19. Wei, X. et al. Oxygen vacancy-mediated selective C-N coupling toward electrocatalytic urea synthesis. *J. Am. Chem. Soc.* **144**, 11530–11535 (2022).
20. Smith, A. T., Plessow, P. N. & Studt, F. Density functional theory calculations of diffusion barriers of organic molecules through the 8-ring of H-SSZ-13. *Chem. Phys.* **541**, 111033 (2021).
21. Rosei, F. et al. Properties of large organic molecules on metal surfaces. *Prog. Surf. Sci.* **71**, 95–146 (2003).
22. Wang, C. et al. Bimetallic $Cu_{11}Ag_3$ nanotips for ultrahigh yield rate of nitrate-to-ammonium. *Angew. Chem. Int. Ed.* **64**, e202415259 (2025).
23. Zhang, H. et al. Computational and experimental demonstrations of one-pot tandem catalysis for electrochemical carbon dioxide reduction to methane. *Nat. Commun.* **10**, 3340 (2019).
24. Li, Y. et al. Reversible hydrogen acceptor-donor enables relay mechanism for nitrate-to-ammonia electrocatalysis. *Angew. Chem. Int. Ed.* **64**, e202417631 (2025).
25. Li, J.-Y. et al. Remote carbon monoxide spillover improves tandem urea electrosynthesis. *Angew. Chem. Int. Ed.* **64**, e202421266 (2025).
26. Curtis Conner, W., Pajonk, G. M. & Teichner, S. J. *Adv. Catal.* 34, 1-79 (1986).
27. Zhao, T. et al. Improving alkaline hydrogen oxidation through dynamic lattice hydrogen migration in Pd@Pt core-shell electrocatalysts. *Angew. Chem. Int. Ed.* **63**, e202315148 (2024).
28. Li, Y. et al. Hydrogen spillover mechanism at the metal-metal interface in electrocatalytic hydrogenation. *Angew. Chem. Int. Ed.* **63**, e202407810 (2024).
29. Ren, X. et al. Emerging 2D copper-based materials for energy storage and conversion: a review and perspective. *Small* **19**, 2204121 (2023).
30. Fan, J. et al. Spatially confined PdH_x metallenes by tensile strained atomic Ru layers for efficient hydrogen evolution. *J. Am. Chem. Soc.* **145**, 5710–5717 (2023).
31. Zhao, Z. et al. Synthesis of stable shape-controlled catalytically active β-palladium hydride. *J. Am. Chem. Soc.* **137**, 15672–15675 (2015).
32. Fan, J. et al. Interstitial hydrogen atom modulation to boost hydrogen evolution in Pd-based alloy nanoparticles. *ACS Nano* **13**, 12987–12995 (2019).

33. Zhang, J. et al. Stable palladium hydride as a superior anode electrocatalyst for direct formic acid fuel cells. *Nano Energy* **44**, 127–134 (2018).
34. Hanneken, J. W., Baker, D. B., Conradi, M. S. & Eastman, J. A. NMR study of the nanocrystalline palladium-hydrogen system. *J. Alloys Compd.* **330-332**, 714–717 (2002).
35. Zhou, W. & Lee, J. Y. Particle size effects in Pd-catalyzed electrooxidation of formic acid. *J. Phys. Chem. C* **112**, 3789–3793 (2008).
36. Zheng, W. iR compensation for electrocatalysis studies: considerations and recommendations. *ACS Energy Lett.* **8**, 1952–1958 (2023).
37. Gong, C. et al. Selective electrocatalytic synthesis of urea using entangled iron porphyrins in covalent organic frameworks. *Nat. Synth.* **4**, 720–729 (2025).
38. Huang, D.-S. et al. Electrosynthesis of urea by using Fe_2O_3 nanoparticles encapsulated in a conductive metal-organic framework. *Nat. Synth.* **3**, 1404–1413 (2024).
39. Wei, X. et al. Lattice oxygen-driven co-adsorption of carbon dioxide and nitrate on copper: a pathway to efficient urea electrosynthesis. *J. Am. Chem. Soc.* **147**, 6049–6057 (2025).
40. Zhao, C. et al. Tailoring activation intermediates of CO_2 initiates C-N coupling for highly selective urea electrosynthesis. *J. Am. Chem. Soc.* **147**, 8871–8880 (2025).
41. Xu, M. et al. Selective urea electrosynthesis from CO_2 and nitrate on spin-polarized atomically ordered PdCuCo. *Adv. Mater.* **37**, 2505286 (2025).
42. Ahmad, M. et al. Advances in electrocatalytic hydrogen evolution coupled with alcohol and aldehyde oxidation: mechanistic insights and economic feasibility. *Adv. Mater.* **37**, 2502966 (2025).
43. Li, S. et al. Coordination environment tuning of nickel sites by oxyanions to optimize methanol electro-oxidation activity. *Nat. Commun.* **13**, 2916 (2022).
44. Li, L. et al. High-performance methanol electrolysis towards energy-saving hydrogen production: using Cu_2O-Cu decorated Ni_2P nanoarray as bifunctional monolithic catalyst. *Chem. Eng. J.* **454**, 140292 (2023).
45. Yin, S. et al. Methanol-assisted energy-saving hydrogen production over defect-rich perforated PdIn bimetallene. *Chem. Eng. J.* **435**, 134711 (2022).
46. Zhang, Y., Fu, Q., Song, B. & Xu, P. Regulation strategy of transition metal oxide-based electrocatalysts for enhanced oxygen evolution reaction. *Acc. Mater. Res.* **3**, 1088–1100 (2022).
47. Fan, K. et al. Active hydrogen boosts electrochemical nitrate reduction to ammonia. *Nat. Commun.* **13**, 7958 (2022).
48. Hu, Q. et al. Pulsed co-electrolysis of carbon dioxide and nitrate for sustainable urea synthesis. *Nat. Sustain.* **7**, 442–451 (2024).
49. Wei, C. et al. Approaches for measuring the surface areas of metal oxide electrocatalysts for determining their intrinsic electrocatalytic activity. *Chem. Soc. Rev.* **48**, 2518–2534 (2019).
50. Xiong, R., Ren, W., Wang, Z. & Zhang, M. Triphenylphosphine as efficient antidote for the sulfur-poisoning of the Pd/C hydrogenation catalyst. *ChemCatChem* **13**, 548–552 (2021).
51. Pignolet, L. H. et al. Phosphine-stabilized, platinum-gold and palladium-gold cluster compounds and applications in catalysis. *Coordin. Chem. Rev.* **143**, 219–263 (1995).
52. Datka, J. & Kozyra, P. TPD-IR studies of CO desorption from zeolites CuY and CuX. *J. Mol. Struct.* **744-747**, 991–996 (2005).
53. Chang, X., Xiong, H., Lu, Q. & Xu, B. Mechanistic implications of low CO coverage on Cu in the electrochemical CO and CO_2 reduction reactions. *JACS Au* **3**, 2948–2963 (2023).
54. Chang, X. et al. Understanding the complementarities of surface-enhanced infrared and Raman spectroscopies in CO adsorption and electrochemical reduction. *Nat. Commun.* **13**, 2656 (2022).
55. Shaaban, E. & Li, G. Probing active sites for carbon oxides hydrogenation on Cu/TiO_2 using infrared spectroscopy. *Commun. Chem.* **5**, 32 (2022).
56. Eischens, R. P. Infrared spectra of chemisorbed molecules. *Acc. Chem. Res.* **5**, 74–80 (1972).
57. Kindness, A. & Marr, I. L. Measurement of carbon-13: carbon-12 ratios by Fourier transform infrared spectrometry. *Analyst* **121**, 205–209 (1996).
58. Šimpraga, R., Tremiliosi-Filho, G., Qian, S. & Conway, B. In situ determination of the 'real are factor' in H_2 evolution electrocatalysis at porous Ni-Fe composite electrodes. *J. Electroanal. Chem.* **424**, 141–151 (1997).
59. Damian, A. & Omanovic, S. Ni and NiMo hydrogen evolution electrocatalysts electrodeposited in a polyaniline matrix. *J. Power Sources* **158**, 464–476 (2006).
60. Li, J. et al. A fundamental viewpoint on the hydrogen spillover phenomenon of electrocatalytic hydrogen evolution. *Nat. Commun.* **12**, 3502 (2021).
61. Comninellis, C. Electrocatalysis in the electrochemical conversion/combustion of organic pollutants for waste water treatment. *Electrochim. Acta* **39**, 1857–1862 (1994).
62. Zhao, T. et al. Functionalizing Cu nanoparticles with fluoric polymer to enhance C_{2+} product selectivity in membraned CO_2 reduction. *Appl. Catal. B Environ.* **340**, 123281 (2024).
63. Jeffrey, H., Marco, D. & Bingjun, X. CO_2 reduction on Cu at low overpotentials with surface-enhanced in situ spectroscopy. *J. Phys. Chem. C* **120**, 17334–17341 (2016).
64. Hunsche, S. et al. OH/OD-IR absorption bands in $SrBa_{1-x}Nb_2O_6$. *Phys. Status Solidi A* **148**, 629–634 (1995).
65. Wu, Q. et al. Surface intermediates steer the pathways of CO_2 hydrogenation on Pt/γ-Al_2O_3: importance of the metal-support interface. *J. Catal.* **425**, 40–49 (2023).
66. Wu, Y., Liu, C., Wang, C., Lu, S. & Zhang, B. Selective transfer semihydrogenation of alkynes with $H_2O(D_2O)$ as the H(D) source over a Pd-P cathode. *Angew. Chem. Int. Ed.* **59**, 21170–21175 (2020).
67. Widom, B. Collision theory of chemical reaction rates. *Adv. Chem. Phys.* **5**, 353 (1963).
68. Li, G.-F., Yang, D. & Abel Chuang, P.-Y. Defining Nafion ionomer roles for enhancing alkaline oxygen evolution electrocatalysis. *ACS Catal.* **8**, 11688–11698 (2018).
69. Choi, P., Jalani, N. H. & Datta, R. Thermodynamics and proton transport in Nafion: II. proton diffusion mechanisms and conductivity. *J. Electrochem. Soc.* **152**, E123 (2005).
70. Kresse, G. & Furthmüller, J. Efficiency of ab-initio total energy calculations for metals and semiconductors using a plane-wave basis set. *Comput. Mater. Sci.* **6**, 15–50 (1996).
71. Kresse, G. & Furthmüller, J. Efficient iterative schemes for ab initio total-energy calculations using a plane-wave basis set. *Phys. Rev. B* **54**, 11169–11186 (1996).
72. Blöchl, P. E. Projector augmented-wave method. *Phys. Rev. B* **50**, 17953–17979 (1994).
73. Perdew, J. P., Burke, K. & Ernzerhof, M. Generalized gradient approximation made simple. *Phys. Rev. Lett.* **77**, 3865–3868 (1996).
74. Grimme, S., Antony, J., Ehrlich, S. & Krieg, H. A consistent and accurate ab initio parametrization of density functional dispersion correction (DFT-D) for the 94 elements H-Pu. *J. Chem. Phys.* **132**, 154104 (2010).
75. Monkhorst, H. J. & Pack, J. D. Special points for Brillouin-zone integrations. *Phys. Rev. B* **13**, 5188–5192 (1976).
76. Wang, V., Xu, N., Liu, J.-C., Tang, G. & Geng, W.-T. VASPKIT: A user-friendly interface facilitating high-throughput computing and analysis using VASP code. *Comput. Phys. Commun.* **267**, 108033 (2021).

77. Tang, Q. & Jiang, D.-E. Mechanism of hydrogen evolution reaction on 1T-MoS_2 from first principles. *ACS Catal.* **6**, 4953–4961 (2016).

Acknowledgements

We acknowledge financial support from the National Key Research and Development Program of China (2024YFE0211200), National Natural Science Foundation of China (Grant 22572156, 22302158 and 22408261), and the Research Plan of International Collaboration Fund for Creative Research Teams (ICFCRT) of NSFC (No. W2441008), the open research fund of Suzhou Laboratory (No. SZLAB-1308-2024-ZD010). B. Han acknowledges the Shanxi Provincial Basic Research Program-Free Exploration Category (No. 202203021212201). R. Zhang acknowledges the Key Projects Supported by the Regional Innovation and Development Joint Fund of the National Natural Science Foundation of China (U23A20132).

Author contributions

Jiayuan Li, Bao Yu Xia, Chen Yu and Yuefei Li conceived the idea, designed the experiments, conducted the characterizations, analyzed the results, and drafted the manuscript. Yurong Liu, Bingying Han, Ye Liu, Baojun Wang and Riguang Zhang contributed to the DFT calculations.

Competing interests

The authors declare no competing interests.

Additional information

Supplementary information The online version contains supplementary material available at https://doi.org/10.1038/s41467-026-69307-1.

Correspondence and requests for materials should be addressed to Yu Chen, Bao Yu Xia or Jiayuan Li.

Peer review information *Nature Communications* thanks Liang Wang, and the other anonymous reviewer(s) for their contribution to the peer review of this work. A peer review file is available.